Journal of
Materials Chemistry A

ROYAL SOCIETY
OF CHEMISTRY

COMMUNICATION

View Article Online
View Journal | View Issue

Check for updates

Cite this: *J. Mater. Chem. A*, 2020, **8**, 4735

Received 10th December 2019
Accepted 16th February 2020

DOI: 10.1039/c9ta13485a

rsc.li/materials-a

Surface oxidized two-dimensional antimonene nanosheets for electrochemical ammonia synthesis under ambient conditions†

Munkhjargal Bat-Erdene, ‡[a] Guangrui Xu,‡[bc] Munkhbayar Batmunkh, [ad] Abdulaziz S. R. Bati, [a] Jessica J. White,[d] Md J. Nine, [e] Dusan Losic, [e] Yu Chen, [c] Yun Wang, [d] Tianyi Ma [b] and Joseph G. Shapter *[a]

Two-dimensional (2D) antimonene nanosheets are prepared using a combination of ball milling and sonication-based liquid exfoliation and are used as an efficient electrocatalyst for the nitrogen reduction reaction (NRR). In 0.1 M KOH, a high NH_3 yield of 180.4 μg h^{-1} mg_{CAT}^{-1} and faradaic efficiency (FE) of 11.6% are achieved using our antimonene nanosheets. Theoretical calculations suggest that the oxidized species of antimonene act as the active catalytic sites for the NRR process. This work opens up a new avenue towards the development of 2D electrocatalysts for clean energy.

Ammonia (NH_3) is one of the most produced chemical materials in the world owing to its importance in various sectors including agriculture, medicine, mining and in the household.[1] NH_3 has also drawn increasing attention as a promising energy carrier with high hydrogen density and low liquefying pressure.[2] Although today's NH_3 production requirements (>150 million tons per year) are principally met by the massive chemical plants based on Haber–Bosch process, this energy-intensive process consumes up to 5% of the global natural gas supply and is also responsible for a large amount of CO_2 emission.[3–5] These issues have led to significant efforts focused on finding alternative methods that are energy-efficient and environmentally friendly to produce NH_3.[6]

Electrocatalytic nitrogen (N_2) reduction reaction (NRR) driven by renewable energy sources offers a promising green process for sustainable production of NH_3 under ambient conditions.[7–9] Of particular importance in the NRR process is to sufficiently activate the N≡N triple bond using efficient catalysts.[7,10,11] Ideal catalytic materials should possess high electrocatalytic activity and selectivity, while still being abundantly available at low-cost. Noble metal catalysts (*e.g.*, Au,[12] Ag,[13] Ru,[14] and Rh[15]) have been the materials of choice for the NRR process. However, the scarcity and high cost of these catalysts hinder their widespread applications. Over the past few years, much attention has been paid to the development of non-noble-metal and metal-free catalysts such as Fe_2O_3–CNT,[16] MoO_3,[17] Li^+ incorporated PEBCD,[18] $Bi_4V_2O_{11}/CeO_2$,[19] N-doped porous carbon.[20]

Two-dimensional (2D) layered nanostructures have attracted increasing attention for use as electrocatalysts for the NRR.[4,5,10,21–23] For instance, Zhang *et al.*[5] explored MoS_2 nanosheets as a noble-metal-free electrocatalyst for the NRR under ambient conditions. This MoS_2 catalyst achieved a faradaic efficiency (FE) of 1.17% at −0.5 V *versus* reversible hydrogen electrode (RHE) in 0.1 M Na_2SO_4. Qiu *et al.*[4] found that boron carbide (B_4C) nanosheets can act as an excellent metal-free electrocatalyst toward NRR for NH_3 synthesis, with a NH_3 production yield of 26.57 μg h^{-1} mg_{CAT}^{-1} and a FE of 15.95% at −0.75 V *versus* RHE when tested in 0.1 M hydrochloric acid (HCl). Recently, Zhang and coworkers used phosphorene nanosheets as a metal-free single element electrocatalyst for NRR.[10] They used both indophenol blue and $^{15}N_2$ isotope labelling methods to determine the NH_3 yield. Intrinsic active sites of phosphorene facilitates the chemisorption of N_2 molecules and provide sufficient electrons for activation of the inert N≡N triple bond. Despite these great advances, the search for novel electrocatalysts that are readily available and exhibit high catalytic properties is still a very active area of research.

Herein, for the first time, we demonstrate that few-layer antimonene (FL-Sb) nanosheets prepared using a liquid-phase exfoliation (LPE) method can be an efficient NRR

---

[a] Australian Institute for Bioengineering and Nanotechnology, The University of Queensland, Brisbane, Queensland 4072, Australia. E-mail: j.shapter@uq.edu.au

[b] Discipline of Chemistry, School of Environmental and Life Sciences, The University of Newcastle (UON), Callaghan, New South Wales 2308, Australia

[c] Key Laboratory of Macromolecular Science of Shaanxi Province, Key Laboratory of Applied Surface and Colloid Chemistry (Ministry of Education), Shaanxi Key Laboratory for Advanced Energy Devices, School of Materials Science and Engineering, Shaanxi Normal University, Xi'an 710062, PR China

[d] Centre for Clean Environment and Energy, School of Environment and Science, Griffith University, Gold Coast, Queensland 4222, Australia

[e] School of Chemical Engineering and Advanced Materials, The University of Adelaide, Adelaide, South Australia 5005, Australia

† Electronic supplementary information (ESI) available. See DOI: 10.1039/c9ta13485a

‡ These two authors made an equal contribution to this work.

electrocatalyst for NH_3 synthesis under ambient conditions. Previous studies found that 2D antimonene can be used as efficient catalyst for electrocatalytic water splitting.[24–26] In our work, when tested in 0.1 M KOH electrolyte, our FL-Sb nanosheets without any supporting catalyst delivered a high NH_3 yield of 180.4 $\mu g\ h^{-1}\ mg_{CAT}^{-1}$ at a potential of −0.1 V and a FE of 11.6% at a potential of +0.05 V *versus* the reversible hydrogen electrode (RHE). We used density functional theory (DFT) calculations to study the electrocatalytic mechanism for NRR on antimonene derivatives.

FL-Sb nanosheets were prepared in a 4 : 1 isopropanol/water mixture by exfoliating bulk Sb crystals using a combination of ball milling and ultrasonication (see ESI for details†). It is well established that ball milling is a powerful strategy to functionalize 2D materials, creating abundant reactive sites, while it also helps to weaken the van der Waals interactions between the flakes.[27] Moreover, Banks *et al.*[28] found that the use of ball milling step helps to produce high yield homogeneous FL-Sb dispersions. The ball milled Sb flakes were further liquid exfoliated using ultrasonication, followed by centrifugation to obtain a stable dispersion of FL-Sb nanosheets with a concentration of around 0.068 g L^{-1} (as determined by UV-vis spectroscopy), which was much higher than previously reported values (1.74×10^{-3} g L^{-1} and 2.53×10^{-3} g L^{-1})[29,30] including the FL-Sb prepared using a modified LPE involving ball milling (0.014 g L^{-1}).[28] This enhancement in the concentration of FL-Sb dispersion may be due to the fact that our ball milling was conducted using smaller ball size (1 mm) as compared to the previous report (5 mm),[28] which results in more efficient exfoliation of bulk Sb. It should be noted that Gibaja *et al.*[24] recently prepared an antimonene dispersion with a concentration of 0.368 g L^{-1} using a highly optimized production method. Atomic force microscopy (AFM) analysis (Fig. 1a) showed that FL-Sb sheets with flake dimensions in the range of a few hundreds of nanometers were produced due to the mechanochemical process induced by the ball milling.[27,28] We further measured the thickness of our flakes deposited on a silicon substrate (Fig. 1a and S1†). The measured heights of our FL-Sb sheets varied from 4 nm to 17 nm, with an average thickness of 10 nm (Fig. 1b). According to previous studies (considering a monolayer Sb sheet is 0.9 nm thick),[31,32] our sample consists of few layers to multilayers sheets.

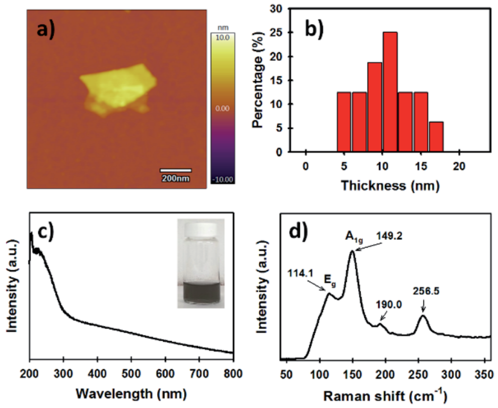

Fig. 1 (a) Representative AFM image of the FL-Sb nanosheet. (b) Histogram of the height (thickness) of the FL-Sb nanosheets measured from 16 individual flakes. (c) UV-vis and (d) Raman spectrum of FL-Sb nanosheets.

As shown in Fig. 1c, the as-prepared FL-Sb dispersion showed a wide UV-vis absorption spectrum, which is consistent with previously reported theoretical results[33] and experimentally measured spectra[30] of 2D Sb. As shown in Fig. 1d, two characteristic Raman peaks centered at 114.1 cm^{-1} (E_g) and 149.2 cm^{-1} (A_{1g}), which can be assigned to the in-plane vibrational mode and out-of-plane vibrational mode, respectively were observed for our FL-Sb and are consistent with the theoretically predicted characteristics of β-phase antimonene.[34] However, the Raman modes centered at 190 cm^{-1} and 256 cm^{-1} were also observed, corresponding to the oxidized states of Sb (Sb_2O_3).[34–36] Interestingly, all these Raman modes including the Sb_2O_3 peaks were also detected for the bulk Sb crystals (Fig. S2†), suggesting that the bulk Sb already had some surface oxidation.

In order to gain further insight into the surface oxidation of both bulk Sb and FL-Sb, X-ray photoelectron spectroscopy (XPS) was used (Fig. 2a and S3a†). As illustrated in Fig. 2b, the high-resolution XPS (Sb 3d) peak of our FL-Sb can be deconvoluted into two main spin-orbit split doublets with splitting of 9.40 eV,[37] in addition to O 1s peak at around 532 eV.[35,36] The small peaks centered at 528.0 eV and 537.4 eV can be assigned to the Sb $3d_{5/2}$ and Sb $3d_{3/2}$ of metallic Sb (Sb^0), while two intense peaks at 530.4 eV and 539.8 eV are attributed to the oxidized Sb (Sb_2O_3).[30,38] This suggests that our FL-Sb samples are strongly oxidized nanosheets and is consistent with previous reports.[38–40] Interestingly, our bulk Sb before exfoliation also showed significant oxidation (Fig. S3b†). Despite this, the Sb_2O_3 peak intensity of the bulk Sb was much lower than that of the FL-Sb, suggesting that further oxidation occurred during the FL-Sb preparation. This further increase in the oxidation of FL-Sb is believed to be due to the use of ball milling, creating abundant reactive sites during the mechanochemical process.[27]

The transmission electron microscopy (TEM) image displayed in Fig. 2c reveals that the lateral size of our FL-Sb nanosheets is around 200 nm which is in agreement with the measured flake size from the AFM images. The lattice spacing of our FL-Sb nanosheet was 0.39 nm (Fig. 2d), which is consistent with previous literature.[39,41] The energy-dispersive X-ray spectroscopy (EDX) elemental mapping illustrated in Fig. 2e–g indicates that our FL-Sb sample contains mainly Sb and O. Furthermore, the EDX spectrum of our FL-Sb exhibited a strong peak for "O" (Fig. 2h), which is an indication of Sb oxidation and consistent with the Raman and XPS results.

NRR experiments were performed in N_2-saturated 0.1 M KOH solution in a gas-tight two-compartment cell under ambient conditions, which was separated by a Nafion membrane. Our FL-Sb nanosheets were used as the cathodic catalyst for the NRR. All potentials were reported on a reversible hydrogen electrode (RHE) scale. The NRR electrocatalytic performance of the FL-Sb nanosheets was first studied a linear

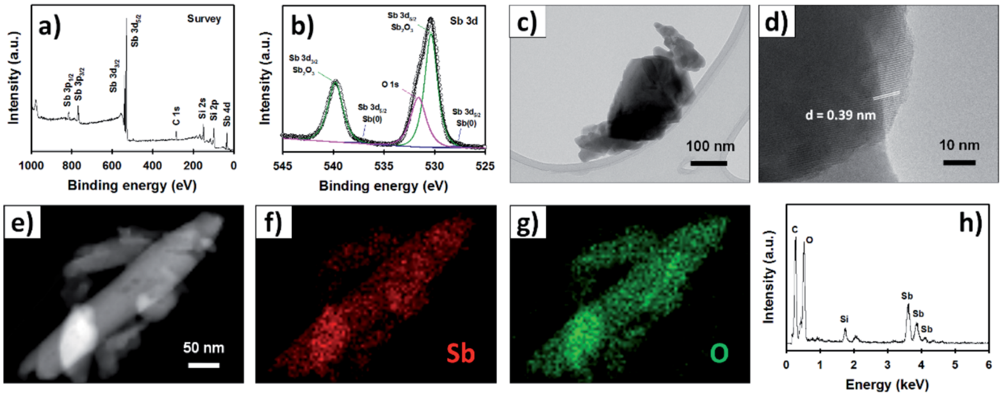

Fig. 2 (a) XPS survey scan, (b) high-resolution Sb 3d spectrum, (c) TEM and (d) HRTEM of FL-Sb nanosheets. (e) High-angle annular dark-field-scanning transmission electron microscope (HAADF-STEM) image of the FL-Sb flakes, and (f and g) the corresponding EDX elemental mapping and (h) EDX spectrum.

sweep voltammetry (LSV) in both N_2-saturated and Ar-saturated 0.1 M KOH solution (Fig. 3a). Although the LSV curves for both Ar- and N_2-saturated solutions showed high current density due to the hydrogen evolution reaction (HER), noticeably higher current density (see Fig. 3a inset) obtained in a N_2-saturated solution indicates that our FL-Sb nanosheets exhibit electrocatalytic activity for the NRR.[42] Chronoamperometry measurements were carried out at different electrode potentials using our FL-Sb nanosheets in N_2-saturated 0.1 M KOH solution. All the chronoamperometric curves showed negligible decay in the catalytic current densities, indicating the excellent stability of our FL-Sb nanosheets (Fig. 3b). It can be clearly seen that the current densities increased at the high electrode potentials due to the dominating HER process in the system.

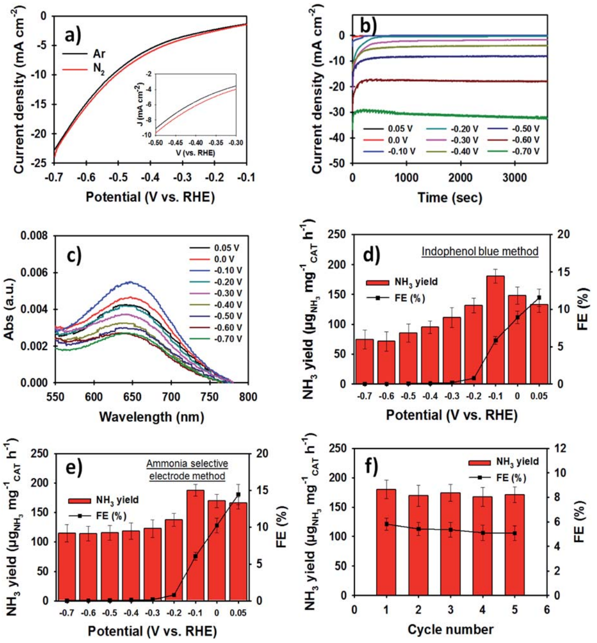

Fig. 3 (a) LSV curves of FL-Sb nanosheets in N_2-saturated and Ar-saturated 0.1 M KOH electrolyte. Inset shows the zoomed in version (*Y*-axis: from −2 to −10 mA cm^{-2}; and *X*-axis: from −0.3 to −0.5 V) of the LSV curve. (b) Chronoamperometric curves of FL-Sb nanosheets in N_2-saturated 0.1 M KOH electrolyte at different potentials. (c) UV-vis absorption spectra of the KOH electrolyte stained with the indophenol indicator after charging at each given potential for 1 h in the presence of FL-Sb catalyst based working electrode, and (d) the corresponding NH_3 yield rate and FE of FL-Sb nanosheets for the NRR (indophenol blue method). (e) NH_3 yield rate and corresponding FE of the FL-Sb nanosheets determined by an ammonia selective electrode. (f) NH_3 yield rate and FE of the FL-Sb nanosheets for the NRR under five consecutive cycles charging at −0.1 V (by indophenol blue method).

The indophenol blue method[43] was used to determine the amount of NH_3 produced (Fig. S4†), and a possible by-product hydrazine (N_2H_4) was detected by the method of Watt and Chrisp (Fig. S5†).[44] Notably, no by-product N_2H_4 was detected (Fig. S6†), suggesting the high selectivity of FL-Sb nanosheets for N_2 toward NH_3 production. After 1 h of the electrocatalytic reaction at constant potentials, the electrolyte containing the NH_3 produced was colored with indophenol indicator and the UV-vis absorption spectra collected (Fig. 3c). The average NH_3 yield and the corresponding FE values were calculated and plotted in Fig. 3d. Clearly, high NH_3 yields and FEs were recorded at the lower potentials, while both the yield and FEs decreased when the potential is below −0.1 V due to the HER process. In particular, our FL-Sb exhibited a maximum NH_3 yield of 180.39 μg h^{-1} mg$_{CAT}^{-1}$ when tested at −0.1 V, and its corresponding FE was 5.8%. The best recorded FE for our FL-Sb was 11.6% when tested at a potential of +0.05 V, while its NH_3 yield was 133.1 μg h^{-1} mg$_{CAT}^{-1}$. The NH_3 yields and FEs obtained for our 2D FL-Sb are remarkable and comparable to the state-of-the-art electrocatalysts including some noble metal containing catalysts.[10,45,46] Table S1† compares the NRR performance obtained by our FL-Sb and other electrocatalysts reported in the literature.

While the indophenol blue is the most widely used method for NH_3 quantification, we also used an ammonia selective electrode as it can provide a much lower detection limit and larger detection range.[47] After plotting a calibration curve (Fig. S7†), the measurements were carried out on the well stabilized electrolyte solution. It can be observed from Fig. 3e that the NH_3 yields and FEs measured using this method were very consistent with the values determined using the indophenol blue method. In order to confirm the fact there is that no contribution to the NH_3 yield from the electrode itself, we carried out NRR experiments using our bare supporting electrode (copper foam (CF)) and tested the yield using both indophenol blue and ammonia selective electrode methods. The yield rates were close to zero at all potentials, confirming that the CF electrode does not contribute to the production of NH_3 during the catalysis (Fig. S8†). We further evaluated the durability of our 2D catalyst for NRR over five consecutive cycles at −0.1 V (*vs.* RHE) (Fig. S9†). As depicted in Fig. 3f, only slight decreases in both the yield rate and FE for NH_3 production was observed after five cycles of chronoamperometric runs (about 90% performance retention at −0.1 V), indicating the robustness of our FL-Sb nanosheets for NRR electrocatalysis.

To identify the active catalytic species of our FL-Sb nanosheets, DFT calculations were carried out. Since the adsorption of N_2 on the catalyst is one of the most important steps for the NRR, the adsorption properties of N_2 both on β-antimonene and Sb_2O_3 (010) surface were analyzed. The β-antimonene was examined to provide a baseline of expected behaviour, while Sb_2O_3 was considered based on the XPS and Raman results obtained. It is well established that Sb_2O_3 consists of molecular units of Sb_4O_6 as shown in Fig. S10 and S11.†[48] By breaking the bonds in the plane (indicated by the dashed green line in Fig. S10†), the (010) surface is formed and used for the calculation. Our theoretical results suggest a weak interaction between N_2 and antimonene. As a comparison, the adsorption energy of N_2 on Sb_2O_3 (010) surface was more than 2 times higher than that on antimonene monolayer (−0.06 and −0.13 eV for antimonene and Sb_2O_3, respectively), which suggests that the Sb_2O_3 is the active catalytic species in our FL-Sb nanosheets. The characterization results show that the topmost layers of antimonene have been oxidized to form Sb_2O_3 so it is clear that these active sites exist in the sample. Moreover, recent theoretical study by Wolff *et al.*[49] reported that oxidized few-layer antimonene forms by itself a heterostructure consisting of semiconducting antimony oxide and semimetallic few-layer antimonene. The stronger adsorption can be ascribed to the increased polarity of Sb_2O_3 with respect to the non-polar antimonene monolayer. The strong adsorption on Sb_2O_3 (010) surface is further evidenced by the charge density difference plots, as shown in Fig. 4. There is almost no charge transfer between N_2 and antimonene due to the considerably weak interaction. On the Sb_2O_3 (010) surface, partial charge is transferred from the N_2 molecules to the region between adsorbate and surface after the adsorption. The transferred charges suggest the activation of the N≡N triple bond, which is beneficial to the NRR.

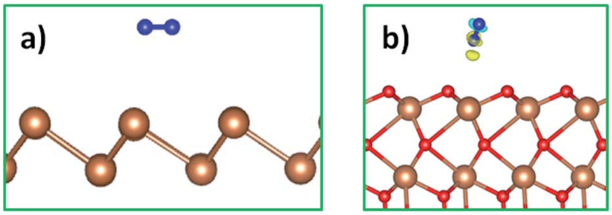

Fig. 4 Charge density difference of systems with adsorbed N_2 molecule on (a) antimonene monolayer and (b) Sb_2O_3 (010) surface. The yellow and cyan contours indicate the enriched and depleted charge densities with the charge density value of $\pm 0.001|e|$ Å^{-3}, respectively. Color code: brown for Sb, red for O and dark blue for N.

Conclusions

In summary, surface-oxidized FL-Sb nanosheets were theoretically predicted and experimentally confirmed to be an active NRR electrocatalyst for electrochemical NH_3 synthesis. When tested in 0.1 M KOH under ambient condition, our 2D antimonene nanosheets exhibited a high NH_3 yield rate of 180.4 μg h^{-1} mg_{CAT}^{-1} and FE of 11.6%. Due to the increased polarity, the adsorption energy of N_2 on the surface-oxidized antimonene was more favorable as compared to the non-polar antimonene monolayer. As such, we found that the oxidized species of antimonene facilitates the activation of the N≡N triple bond for the NRR process. We anticipate that the results reported in this work could open a new avenue in the development of mono-elemental 2D catalysts for the electrocatalytic synthesis of NH_3.

Conflicts of interest

There are no conflicts to declare.

Acknowledgements

The support of the Australian Research Council Discovery Program (DP160101301) is gratefully acknowledged. We acknowledge the use of the Queensland node of the Australian National Fabrication Facility (ANFF-Q) at the University of Queensland. This research was undertaken on the supercomputers in National Computational Infrastructure (NCI) in Canberra, Australia, which is supported by the Australian Commonwealth Government, and Pawsey Supercomputing Centre in Perth with the funding from the Australian Government and the Government of Western Australia. The authors thank Dr Ashley D. Slattery of Adelaide Microscopy at the University of Adelaide for his help for Titan TEM analysis.

Notes and references

1 B. M. Hoffman, D. Lukoyanov, Z.-Y. Yang, D. R. Dean and L. C. Seefeldt, *Chem. Rev.*, 2014, **114**, 4041–4062.
2 D. J. Little, I. I. I. M. R. Smith and T. W. Hamann, *Energy Environ. Sci.*, 2015, **8**, 2775–2781.
3 R. F. Service, *Science*, 2014, **345**, 610.
4 W. Qiu, X.-Y. Xie, J. Qiu, W.-H. Fang, R. Liang, X. Ren, X. Ji, G. Cui, A. M. Asiri, G. Cui, B. Tang and X. Sun, *Nat. Commun.*, 2018, **9**, 3485.
5 L. Zhang, X. Ji, X. Ren, Y. Ma, X. Shi, Z. Tian, A. M. Asiri, L. Chen, B. Tang and X. Sun, *Adv. Mater.*, 2018, **30**, 1800191.
6 K. A. Brown, D. F. Harris, M. B. Wilker, A. Rasmussen, N. Khadka, H. Hamby, S. Keable, G. Dukovic, J. W. Peters, L. C. Seefeldt and P. W. King, *Science*, 2016, **352**, 448–450.

7 X. Cui, C. Tang and Q. Zhang, *Adv. Energy Mater.*, 2018, **8**, 1800369.
8 X. Guo, H. Du, F. Qu and J. Li, *J. Mater. Chem. A*, 2019, **7**, 3531–3543.
9 G.-F. Chen, S. Ren, L. Zhang, H. Cheng, Y. Luo, K. Zhu, L.-X. Ding and H. Wang, *Small Methods*, 2019, **3**, 1800337.
10 L. Zhang, L.-X. Ding, G.-F. Chen, X. Yang and H. Wang, *Angew. Chem., Int. Ed.*, 2019, **58**, 2612–2616.
11 K. Liu, J. Fu, L. Zhu, X. Zhang, H. Li, H. Liu, J. Hu and M. Liu, *Nanoscale*, 2020, DOI: 10.1039/c9nr09117c.
12 M.-M. Shi, D. Bao, B.-R. Wulan, Y.-H. Li, Y.-F. Zhang, J.-M. Yan and Q. Jiang, *Adv. Mater.*, 2017, **29**, 1606550.
13 H. K. Lee, C. S. L. Koh, Y. H. Lee, C. Liu, I. Y. Phang, X. Han, C.-K. Tsung and X. Y. Ling, *Sci. Adv.*, 2018, **4**, eaar3208.
14 Y. Yao, H. Wang, X.-z. Yuan, H. Li and M. Shao, *ACS Energy Lett.*, 2019, **4**, 1336–1341.
15 H.-M. Liu, S.-H. Han, Y. Zhao, Y.-Y. Zhu, X.-L. Tian, J.-H. Zeng, J.-X. Jiang, B. Y. Xia and Y. Chen, *J. Mater. Chem. A*, 2018, **6**, 3211–3217.
16 S. Chen, S. Perathoner, C. Ampelli, C. Mebrahtu, D. Su and G. Centi, *Angew. Chem., Int. Ed.*, 2017, **56**, 2699–2703.
17 J. Han, X. Ji, X. Ren, G. Cui, L. Li, F. Xie, H. Wang, B. Li and X. Sun, *J. Mater. Chem. A*, 2018, **6**, 12974–12977.
18 G.-F. Chen, X. Cao, S. Wu, X. Zeng, L.-X. Ding, M. Zhu and H. Wang, *J. Am. Chem. Soc.*, 2017, **139**, 9771–9774.
19 C. Lv, C. Yan, G. Chen, Y. Ding, J. Sun, Y. Zhou and G. Yu, *Angew. Chem., Int. Ed.*, 2018, **57**, 6073–6076.
20 Y. Liu, Y. Su, X. Quan, X. Fan, S. Chen, H. Yu, H. Zhao, Y. Zhang and J. Zhao, *ACS Catal.*, 2018, **8**, 1186–1191.
21 X. Yu, P. Han, Z. Wei, L. Huang, Z. Gu, S. Peng, J. Ma and G. Zheng, *Joule*, 2018, **2**, 1610–1622.
22 P. Chen, N. Zhang, S. Wang, T. Zhou, Y. Tong, C. Ao, W. Yan, L. Zhang, W. Chu, C. Wu and Y. Xie, *Proc. Natl. Acad. Sci. U. S. A.*, 2019, **116**, 6635–6640.
23 Y. Luo, G.-F. Chen, L. Ding, X. Chen, L.-X. Ding and H. Wang, *Joule*, 2019, **3**, 279–289.
24 C. Gibaja, M. Assebban, I. Torres, M. Fickert, R. Sanchis-Gual, I. Brotons, W. S. Paz, J. J. Palacios, E. G. Michel, G. Abellán and F. Zamora, *J. Mater. Chem. A*, 2019, **7**, 22475–22486.
25 X. Ren, Z. Li, H. Qiao, W. Liang, H. Liu, F. Zhang, X. Qi, Y. Liu, Z. Huang, D. Zhang, J. Li, J. Zhong and H. Zhang, *ACS Appl. Energy Mater.*, 2019, **2**, 4774–4781.
26 P. Ares, J. J. Palacios, G. Abellán, J. Gómez-Herrero and F. Zamora, *Adv. Mater.*, 2018, **30**, 1703771.
27 J. Xu, I.-Y. Jeon, J.-M. Seo, S. Dou, L. Dai and J.-B. Baek, *Adv. Mater.*, 2014, **26**, 7317–7323.
28 E. Martínez-Periñán, M. P. Down, C. Gibaja, E. Lorenzo, F. Zamora and C. E. Banks, *Adv. Energy Mater.*, 2018, **8**, 1702606.
29 C. Gibaja, D. Rodriguez-San-Miguel, P. Ares, J. Gómez-Herrero, M. Varela, R. Gillen, J. Maultzsch, F. Hauke, A. Hirsch, G. Abellán and F. Zamora, *Angew. Chem., Int. Ed.*, 2016, **55**, 14345–14349.
30 F. Zhang, J. He, Y. Xiang, K. Zheng, B. Xue, S. Ye, X. Peng, Y. Hao, J. Lian, P. Zeng, J. Qu and J. Song, *Adv. Mater.*, 2018, **30**, 1803244.
31 P. Ares, F. Aguilar-Galindo, D. Rodríguez-San-Miguel, D. A. Aldave, S. Díaz-Tendero, M. Alcamí, F. Martín, J. Gómez-Herrero and F. Zamora, *Adv. Mater.*, 2016, **28**, 6332–6336.
32 F. Li, M. Xue, J. Li, X. Ma, L. Chen, X. Zhang, D. R. MacFarlane and J. Zhang, *Angew. Chem., Int. Ed.*, 2017, **56**, 14718–14722.
33 N. Wang, D. Cao, J. Wang, P. Liang, X. Chen and H. Shu, *J. Mater. Chem. C*, 2017, **5**, 9687–9693.
34 J. Ji, X. Song, J. Liu, Z. Yan, C. Huo, S. Zhang, M. Su, L. Liao, W. Wang, Z. Ni, Y. Hao and H. Zeng, *Nat. Commun.*, 2016, **7**, 13352.
35 G. Abellán, P. Ares, S. Wild, E. Nuin, C. Neiss, D. R.-S. Miguel, P. Segovia, C. Gibaja, E. G. Michel, A. Görling, F. Hauke, J. Gómez-Herrero, A. Hirsch and F. Zamora, *Angew. Chem., Int. Ed.*, 2017, **56**, 14389–14394.
36 V. Lloret, M. Á. Rivero-Crespo, J. A. Vidal-Moya, S. Wild, A. Doménech-Carbó, B. S. J. Heller, S. Shin, H.-P. Steinrück, F. Maier, F. Hauke, M. Varela, A. Hirsch, A. Leyva-Pérez and G. Abellán, *Nat. Commun.*, 2019, **10**, 509.
37 E. N. K. Glover, S. G. Ellington, G. Sankar and R. G. Palgrave, *J. Mater. Chem. A*, 2016, **4**, 6946–6954.
38 R. Gusmão, Z. Sofer, D. Bouša and M. Pumera, *Angew. Chem., Int. Ed.*, 2017, **56**, 14417–14422.
39 C. C. Mayorga-Martinez, R. Gusmão, Z. Sofer and M. Pumera, *Angew. Chem., Int. Ed.*, 2019, **58**, 134–138.
40 Y. Gao, W. Tian, C. Huo, K. Zhang, S. Guo, S. Zhang, X. Song, L. Jiang, K. Huo and H. Zeng, *J. Mater. Chem. A*, 2019, **7**, 3238–3243.
41 X. Wang, J. He, B. Zhou, Y. Zhang, J. Wu, R. Hu, L. Liu, J. Song and J. Qu, *Angew. Chem., Int. Ed.*, 2018, **57**, 8668–8673.
42 H. Jin, L. Li, X. Liu, C. Tang, W. Xu, S. Chen, L. Song, Y. Zheng and S.-Z. Qiao, *Adv. Mater.*, 2019, **31**, 1902709.
43 D. Zhu, L. Zhang, R. E. Ruther and R. J. Hamers, *Nat. Mater.*, 2013, **12**, 836.
44 G. W. Watt and J. D. Chrisp, *Anal. Chem.*, 1952, **24**, 2006–2008.
45 X. Zhang, T. Wu, H. Wang, R. Zhao, H. Chen, T. Wang, P. Wei, Y. Luo, Y. Zhang and X. Sun, *ACS Catal.*, 2019, **9**, 4609–4615.
46 L. Li, C. Tang, B. Xia, H. Jin, Y. Zheng and S.-Z. Qiao, *ACS Catal.*, 2019, **9**, 2902–2908.
47 C. Tang and S.-Z. Qiao, *Chem. Soc. Rev.*, 2019, **48**, 3166–3180.
48 C. Svensson, *Acta Crystallogr., Sect. B: Struct. Crystallogr. Cryst. Chem.*, 1975, **31**, 2016–2018.
49 S. Wolff, R. Gillen, M. Assebban, G. Abellán and J. Maultzsch, [Cond-mat.mtrl-sci], 2019, arXiv:1909.01204v01203.